



Deposited via The University of Leeds.

White Rose Research Online URL for this paper:

<https://eprints.whiterose.ac.uk/id/eprint/94254/>

Version: Accepted Version

Article:

Nissen, E, Elliott, JR, Sloan, RA et al. (2016) Limitations of rupture forecasting exposed by instantaneously triggered earthquake doublet. *Nature Geoscience*, 9 (4). pp. 330-336.

ISSN: 1752-0894

<https://doi.org/10.1038/ngeo2653>

Reuse

Items deposited in White Rose Research Online are protected by copyright, with all rights reserved unless indicated otherwise. They may be downloaded and/or printed for private study, or other acts as permitted by national copyright laws. The publisher or other rights holders may allow further reproduction and re-use of the full text version. This is indicated by the licence information on the White Rose Research Online record for the item.

Takedown

If you consider content in White Rose Research Online to be in breach of UK law, please notify us by emailing eprints@whiterose.ac.uk including the URL of the record and the reason for the withdrawal request.

Limitations of rupture forecasting exposed by instantaneously triggered earthquake doublet

E. Nissen¹, J. R. Elliott², R. A. Sloan^{2,3}, T. J. Craig⁴, G. J. Funning⁵, A. Hutko⁶, B. E. Parsons², T. J. Wright⁴

¹ Department of Geophysics, Colorado School of Mines, 1500 Illinois Street, Golden, CO 80401.

USA

² COMET, Department of Earth Sciences, University of Oxford, South Parks Road, Oxford OX1

3AN, UK

³ Department of Geological Sciences, University of Cape Town, Private Bag X3, Rondebosch

7701, South Africa

⁴ COMET, School of Earth and Environment, University of Leeds, Leeds LS2 9JT, UK

⁴ Department of Earth Sciences, University of California, Riverside, CA 92521, USA

⁵ Incorporated Research Institutions for Seismology (IRIS) Data Management Center, 1408 NE

45th St, Suite 201, Seattle, WA 98105, USA

Earthquake hazard assessments and rupture forecasts are based on the potential length of seismic rupture and whether or not slip is arrested at fault segment boundaries. Such forecasts do not generally consider that one earthquake can trigger a second large event, near-instantaneously, at distances greater than a few kilometers. Here we present a geodetic and seismological analysis of a magnitude 7.1 intra-continental earthquake that occurred in Pakistan in 1997. We find that the earthquake, rather than a single event as hitherto assumed, was in fact an earthquake doublet: initial rupture on a shallow, blind

reverse fault was followed just 19 seconds later by a second rupture on a separate reverse fault 50 km away. Slip on the second fault increased the total seismic moment by half, and doubled both the combined event duration and the area of maximum ground shaking. We infer that static Coulomb stresses at the initiation location of the second earthquake were probably reduced as a result of the first. Instead, we suggest that a dynamic triggering mechanism is likely, although the responsible seismic wave phase is unclear. Our results expose a flaw in earthquake rupture forecasts that disregard cascading, multiple-fault ruptures of this type.

Continental earthquakes typically rupture diffuse systems of shallow fault segments, delineated by bends, step-overs, gaps, and terminations. The largest events generally involve slip on multiple segments, and whether or not rupture is arrested by these boundaries can determine the difference between a moderate earthquake and a potentially devastating one. Compilations of historical surface ruptures suggest that boundary offsets of ~ 5 km are sufficient to halt earthquakes, regardless of the total rupture length^{1,2}. This value is incorporated into modern, fault-based earthquake rupture forecasts such as the UCERF3 model for California^{3,4}, whose goals include anticipating the maximum possible rupture length and magnitude of future earthquakes within known fault systems.

However, if earthquakes could rapidly trigger failure of neighbouring faults or fault segments, at distances larger than ~ 5 km, then such scenario planning could be missing an important class of cascading, multiple-fault rupture. Here we exploit the combination of spatial

information captured by satellite deformation measurements and timing information of successive fault ruptures from seismology, to reveal how near-instantaneous, probably dynamic triggering may lead to sequential rupture of multiple large earthquakes separated by distances of 10s of kilometers.

The destructive Harnai earthquake occurred on 27 February 1997 at 21:08 UTC (02:08 on 28 February, local time) in the western Sulaiman mountains of Pakistan⁵ (Figure 1a). Published source catalogues ascribe it a single, largely (85% – 99%) double-couple focal mechanism with gentle ~N-dipping and steep ~S-dipping nodal planes and a moment magnitude M_w of 7.0 – 7.1 (Supplementary Table 1). The largest catalogued aftershocks include a M_s 6.4 event that struck 22 minutes after the mainshock at 21:30 UTC, and seven further earthquakes of $M > 5.0$ during the next ten months. There were no reports of surface rupturing in any of these events. The Sulaiman mountains lie within the western boundary zone of the India-Eurasia collision where Paleozoic–Paleogene Indian passive margin sediments and Neogene flysch and molasse are folded and thrust over rigid Indian basement⁶⁻⁹ (inset, Figure 1a; Supplementary Figure 1). Cover thicknesses increase from 8 – 10 km within the low-lying Sibi Trough, south of the range, to 15 – 20 km in the range interior¹⁰⁻¹². Past instrumental seismicity is dominated by reverse faulting earthquakes with centroid depths of < 10 km, steeply-dipping (30° – 60°) nodal planes roughly aligned with local surface folding, and P-axes oriented radially to the curved mountain front as if gravitational forces arising from the topography are important in driving deformation^{8,10,13-16}.

Surface deformation from InSAR

We mapped the surface deformation in the Harnai earthquake with Interferometric Synthetic Aperture Radar (InSAR), using two images captured on 6 May 1996 and 31 May 1999 by the European Space Agency (ESA) European Resource Satellite (ERS-2) satellite (see Methods). The descending-track satellite line-of-sight has an azimuth of 283° and is inclined at 23° from the vertical at the scene centre. The interferogram (Figure 1b) contains a near-continuous signal in mountainous areas but is decorrelated over most of the Sibi Trough, probably due to agriculture. It contains two distinct fringe ellipses containing displacements toward the satellite, characteristic of slip on buried thrust or reverse faults: one in the scene centre and one in the south-eastern corner of the interferogram. The unwrapped interferogram contains peak displacements of ~ 60 cm toward the satellite in the central deformation patch and ~ 50 cm toward the satellite in the south-eastern one (Figure 1c). The south-eastern fringe pattern is partially obscured by an incoherent region where high deformation gradients or mass movements may have caused decorrelation.

To characterize the causative faulting we used elastic dislocation modelling^{17,18} guided where possible by independent constraints from seismology (see Methods). The broad fringe ellipse in the scene centre corresponds to slip on a buried, NNE-dipping, shallow-angle (21°) reverse fault (labelled F1 in Figure 1d - e) with a moment magnitude of 7.0. Slip is centred at a depth of ~ 15 km, consistent with the estimated depth of the basement-sedimentary cover interface in this area¹². Seismic slip along this interface would rule out the existence of a weak

decollement of the kind that underlies the lobate Sulaiman range to the East. Whereas the apex of the Sulaiman range can propagate southwards, facilitated by foreland sediments that are weaker and/or thicker than in neighbouring parts of the Indian plate^{8,10,15,16}, partial coupling of basement and cover rocks may instead enable the Indian basement to drag the cover northwards, generating the sharp syntaxis around the Sibi Trough (inset, Figure 1a). Similar correspondences between low-angle thrusting and local absence of salt are observed within syntaxes and embayments of other active fold-thrust belts in south Asia¹⁹⁻²¹.

The south-eastern fringe ellipse is caused by slip on another NE-dipping reverse fault (labelled F2 in Figure 1d, e) with a moment magnitude of 6.8. The F2 fault is spatially distinct from F1, being offset southwards, steeper (dip 31°), and shallower (slip is centered at ~ 9 km, within the sedimentary cover rather than along the basement interface), and there is no indication of any slip connecting the two structures. F2 coseismic uplift is centred along the prominent Tadri anticline (Figure 1a), which may be a fault propagation or fault bend fold controlled by underlying reverse slip.

We also find that additional reverse slip totalling M_w 6.1 on a third, subsidiary structure (labelled F3 in Figure 1d – e) is required to fit a minor E-W phase discontinuity in the southern part of the central fringe pattern. However, its shallow depth extents (0 – 5 km), elongate dimensions (~ 20 km) and close spatial correspondence with steep, overturned strata belonging to the southern limb of the Khand Sepal anticline (Figure 1a), suggest that it represents minor bedding plane slip rather than primary earthquake faulting. This

deformation resembles after-slip observed along small faults and folds within the hanging-walls of a cluster of larger earthquakes near Sefidabeh in Iran²², and we suspect that slip associated with model fault F3 also occurred post-seismically.

Timing and spacing of seismic slip from arrival times

The InSAR models capture the cumulative surface deformation between May 1996 and May 1999, but what are the relative contributions from seismic slip in the 27 February 1997 earthquake, subsequent aftershocks, and aseismic afterslip? We use seismology to help disentangle the temporal evolution of the signals contained in the interferogram and to provide independent constraints on fault geometry.

With no local network in place, we are restricted to using Global Seismographic Network seismograms at teleseismic distances, augmented by a few regional stations. Teleseismic broadband, vertical component seismograms (Figure 2a) indicate an abrupt, positive (upwards) arrival that postdates the initial *P*-wave by 16 – 17 seconds at eastern and south-eastern azimuths, by 18 – 20 seconds at northern and north-eastern azimuths, and by 21 – 22 seconds at western and north-western azimuths. This azimuthal variation is consistent with a second earthquake that initiates south-east of the first after a delay of ~19 seconds. Henceforth, we refer to these two, distinct events as the Harnai mainshock and +19 second aftershock. It is difficult to identify the second arrival at south-western azimuths, where stations lie close to the SW-dipping auxiliary plane of the InSAR-derived F2 focal sphere (Figure

2b); at southern azimuths, stations are located on ocean islands and detection is hampered by oceanic noise.

We used a multiple-earthquake relocation technique^{23,24} to better define the spatial relationship between the epicentres of the mainshock, the +19 second earthquake, and later aftershocks (Figure 2b; see Methods). To calibrate the cluster we exploited the 9 December 2008 Ziarat earthquake (M_w 5.7) which occurred in the north-western part of Figure 2b, and whose surface trace is known from InSAR²⁵⁻²⁷. The relocated mainshock epicentre lies at the south-eastern end of the F1 model fault (12 – 14 km south of the published catalogue epicentres), indicating that this fault ruptured first. The epicentral location with respect to the surface deformation implies that mainshock slip then propagated north-westwards along the F1 fault, generating the broad InSAR signal in the centre of the interferograms. The relocated +19 second aftershock epicentre lies ~50 km SE of the mainshock epicentre near the south-eastern end of the F2 fault, at a location in which model slip is restricted to depths of 11 – 17 km (Figure 1e). To generate the south-eastern fringe ellipse, the +19 second event must then have ruptured unilaterally towards the NW and from near the bottom upwards.

Later aftershocks are mostly concentrated within or around the edges of the two main fringe ellipses in the interferograms, though of these only the 27 February 21:30 UTC (M_s 6.4) earthquake is probably large enough to have made a significant contributions to the InSAR deformation. It occurred west of the mainshock hypocentre and may have ruptured or re-ruptured the western part of the F1 slip patch, though we have no independent constraints on

its mechanism. Hypocentre locations and source parameters obtained from modelling long-period teleseismic body-waveforms^{19,28} (see Methods) indicate that the 20 March (M_w 5.6), 17 June (M_w 5.0), 24 August (M_w 5.5) and 7 September 1997 (M_w 5.3) aftershocks probably ruptured the down-dip extension of the Harnai mainshock fault plane (Figure 2b). Crucially, the largest catalogued aftershock associated with the south-eastern fringe ellipse is just m_b 5.1 and is thus much too small to have generated the surface deformation associated with the F2 fault (M_w 6.8). This discounts a later aftershock as the cause of the F2 faulting.

Timing, spacing and scaling of seismic slip from back-projections

Seismic back-projections confirm our proposed model of the spatial and temporal relationship between the Harnai mainshock and +19 second aftershock and provide independent seismological evidence in favour of their comparable magnitudes. Using two dense arrays of teleseismic broadband stations centred in Europe (Figure 3a) and North America (Figure 3d), we back-projected coherent P -wave energy onto a grid surrounding the source region over a 2 minute period spanning both the mainshock and aftershock^{29, 30}. Both back-projections show two distinct peaks in stacked energy, separated by ~18 seconds (Figure 3b, 3e; Supplementary Videos 1, 2). The two peaks have very similar shapes and amplitudes, consistent with comparable moment release in each event. Spatially, the distance and azimuth between the two peaks (31 km and 135° for the EU back-projection, and 41 km and 146° for the North American back-projection) are consistent with those separating the InSAR-derived F1 and F2 model fault centre coordinates (49 km and 141°). This rules out aseismic afterslip as the

source of the south-eastern deformation lobe, since this would leave the second, south-eastern peak in seismic radiation completely unaccounted for.

Triggering mechanism

We have established that the M_w 7.0 Harnai mainshock was followed ~19 seconds later by a M_w 6.8 aftershock, initiating ~50 km to the SE on a spatially distinct fault, but what is the causal relationship between the two earthquakes?

Firstly, we investigate whether permanent (static) stress changes, imparted by mainshock fault slip upon the surrounding medium once the seismic vibrations have ceased, promoted failure of the aftershock fault, which was presumably also late in its earthquake cycle and critically stressed³¹. We calculated the static Coulomb failure stress change on the aftershock (“receiver”) fault caused by slip on the mainshock (“source”) fault³², using the F2 and F1 fault plane parameters, preferred F1 slip distribution, and the same elastic moduli as in our InSAR modelling. Positive Coulomb stresses mean that receiver faults are brought closer to failure (through an increase in shear stresses and/or a decrease in normal stresses), whilst negative Coulomb stresses mean that receiver faults are brought further from failure. Coulomb stresses beneath the aftershock epicentre are negative over its inferred nucleation depth range of 11 – 16 km (Figure 4a), with a value of -0.003 MPa at the minimum-misfit hypocentre location itself (Figure 4b).

To test the robustness of this result, we repeated the calculation using perturbed source and receiver fault orientations and source slip distributions. Fault strikes, dips and rakes were varied within their formal error bounds, and alternative source fault slip distributions were generated using a range of slip smoothing factors (see Methods and Supplementary Figures 3 – 5). Perturbing either the source fault parameters or slip distribution has no discernible impact on Coulomb stress changes at the aftershock hypocentre. Changing the receiver fault orientation has a larger effect (Supplementary Figure 6), in some instances raising the Coulomb stresses at the aftershock hypocentre to as much as -0.001 MPa, but never to positive values. We also investigated the temporal progression in static stress change on the aftershock fault, by determining static Coulomb stresses generated by each 2-second increment in accumulated F1 slip. Assuming a unilateral F1 rupture propagating from SE to NW at 2.5 km/s (see Methods), we find that Coulomb stress changes at the aftershock hypocentre are negative for the complete duration of F1 rupture (Supplementary Figure 7).

Although certain limitations to our modelling – namely assumptions of planar faults with uniform rake embedded within a uniform elastic half-space – do not permit us to definitively rule out small, positive Coulomb stresses at the location of aftershock initiation, all available evidence therefore suggests that static stresses imparted by mainshock slip on the F1 fault brought the aftershock fault further from failure, not closer. This implies instead that the +19 second aftershock was triggered instead by transient (dynamic) stresses generated by the passing seismic waves.

We have no direct constraints on seismic velocities in the sequence of cover rocks above and between the F1 and F2 faults, but we can place conservative bounds of 4 – 7 km/s for average *P*-wave velocities and 2 – 4 km/s for shear and surface wave velocities. This would indicate that the +19 second aftershock initiated several (~6 – 12) seconds after passage of *P*-waves originating at the mainshock hypocentre, at about the same time as the first *S*-wave and emergent surface wave arrivals, and also at around the same time as passage of *P*-waves generated along the north-western F1 fault.

Of these wave-types, surface waves are most commonly attributed to suspected cases of dynamic triggering due to their larger amplitudes, though body-waves have also been implicated in sequences of deep focus earthquakes³³. Great earthquakes commonly generate both instantaneous and delayed seismicity at distances of hundreds to thousands of kilometres, where static stress changes are negligible, but these remote aftershocks usually have small magnitudes and often occur in volcanic or geothermal areas with quite different stress and frictional regimes³⁴⁻³⁶. A notable exception was a M_w 6.9 earthquake in Japan that initiated during the passage of surface waves from a M_w 6.6 event in Indonesia, confirming the potential for larger triggered earthquakes in compressive environments³⁷. However, whether dynamic triggering also occurs locally (within 1 -2 fault lengths of the triggering event) is still controversial, in part because deconvolving static and transient stress changes within this area is challenging³⁸⁻⁴¹. On the one hand, asymmetric aftershock distributions for earthquakes that exhibit a strong rupture directivity⁴², and raised aftershock rates for impulsive earthquakes compared to aseismic slip events of the same magnitude⁴³, both hint at the occurrence of

dynamic triggering within the source region. On the other hand, the high amplitude surface waves which impart the largest transient stresses only fully emerge at much larger distances, leading to the very feasibility of dynamic triggering in the near-field (10s of kilometres) being questioned⁴⁴.

Our results indicate that large earthquakes can indeed be triggered at such short distances by transient stresses. However, without better constraints on local seismic velocities or any local stations, and given the likelihood of complex wave interactions within the folded and faulted sedimentary cover, we are unable to determine the wave-type responsible for triggering the +19 second aftershock. It is therefore unclear whether reductions in the normal stresses on the aftershock fault, increases in shearing stresses, changes to pore fluid pressure, or a combination of these factors were responsible. Since static stresses are only fully transmitted once the seismic waves have passed by, we cannot establish what proportion of the (negative) static stress change from F1 slip was felt at the aftershock hypocentre at its origin time, and hence we are unable to place even a lower bound on the (positive) dynamic triggering stress.

Compilations of historical surface rupture traces have been used to imply that fault segment gaps of ~5 km are sufficient to halt an earthquake rupture^{1,2}. This figure is also in broad agreement with numerical earthquake simulations⁴⁵. The notion that segment boundaries larger than 5 km will always arrest slip has since been incorporated into the state-of-the-art UCERF3 rupture forecast models for California^{3,4}. Yet a few earthquakes are known to have bridged larger segment boundary distances. Surface traces of the 1932 Chang Ma, China (*M*

~7.6) and 1896 Rikuu, Japan ($M \sim 7.5$) reverse faulting earthquakes contain gaps of 10 km and 15 km, respectively⁴⁶, whilst the complex M_w 8.6 Indian Ocean intraplate earthquake of 11 April 2012 bridged a gap of ~20 km between subparallel, but separate, strike-slip faults⁴⁷. However, these events are much larger than the Harnai earthquake and it is possible that in each case static stresses were sufficiently large to trigger slip at distances of 10 – 20 km.

The Harnai doublet is unprecedented amongst modern, well-recorded events in involving near-instantaneous triggering at a distance of ~50 km, probably through dynamic rather than static stress transfer. The second earthquake increased the eventual seismic moment by ~50% and doubled both the duration of ground shaking and the area affected by the strongest shaking, illustrating the added danger posed by multi-fault ruptures of this type. The implications of this behaviour are especially relevant to other continental fold-and-thrust belts. Earthquake dimensions in these settings are often obscured due to loss of near-surface slip to folding, limiting the value of historical surface rupture catalogues in anticipating earthquake arrest⁴⁵. Since joint geodetic and seismological analyses are not yet standardized, it is unclear how exceptional triggering of the type observed in the Harnai doublet is. A comparison between geological slip rates and historical earthquake occurrence suggests that multi-segment earthquakes with larger-than-expected magnitudes may be rather frequent amongst the reverse faults of the Los Angeles basin and surroundings⁴⁸. Our results indicate that multiple-fault ruptures (as opposed to merely multiple-segment ones), such as sequential failure of the Sierra Madre and Puente Hills thrusts which are separated by ~20 km, are also mechanically feasible if both systems are critically stressed. Rupture forecast models which

prohibit triggering over such length- and time-scales are likely overly optimistic in anticipating earthquake hazard in areas that contain dense networks of active faults.

Correspondence

Correspondence and requests for materials should be addressed to Edwin Nissen (enissen@mines.edu).

Acknowledgments

This work is supported by the UK Natural Environmental Research Council (NERC) through the Looking Inside the Continents project (NE/K011006/1), the Earthquake without Frontiers project (EwF_NE/J02001X/1_1) and the Centre for the Observation and Modelling of Earthquakes, Volcanoes and Tectonics (COMET). The Incorporated Research Institutions for Seismology (IRIS) Data Management Center is funded through the Seismological Facilities for the Advancement of Geoscience and EarthScope (SAGE) Proposal of the National Science Foundation (EAR-1261681). We are grateful to Eric Bergman for guidance in earthquake relocations, Kevin McMullan and Andrew Rickerby for their assistance with preliminary InSAR and body waveform modelling, and three anonymous reviewers and the editor for comments which helped improve the manuscript.

Author contributions

InSAR analysis and accompanying Coulomb modelling was undertaken by E.N. and J.R.E. Seismological analyses were led by R.A.S. (calibrated multi-event relocation), A.H. (seismic

back-projection) and E.N. (body-waveform modelling). All authors contributed to the interpretation of results and E. N. wrote the manuscript.

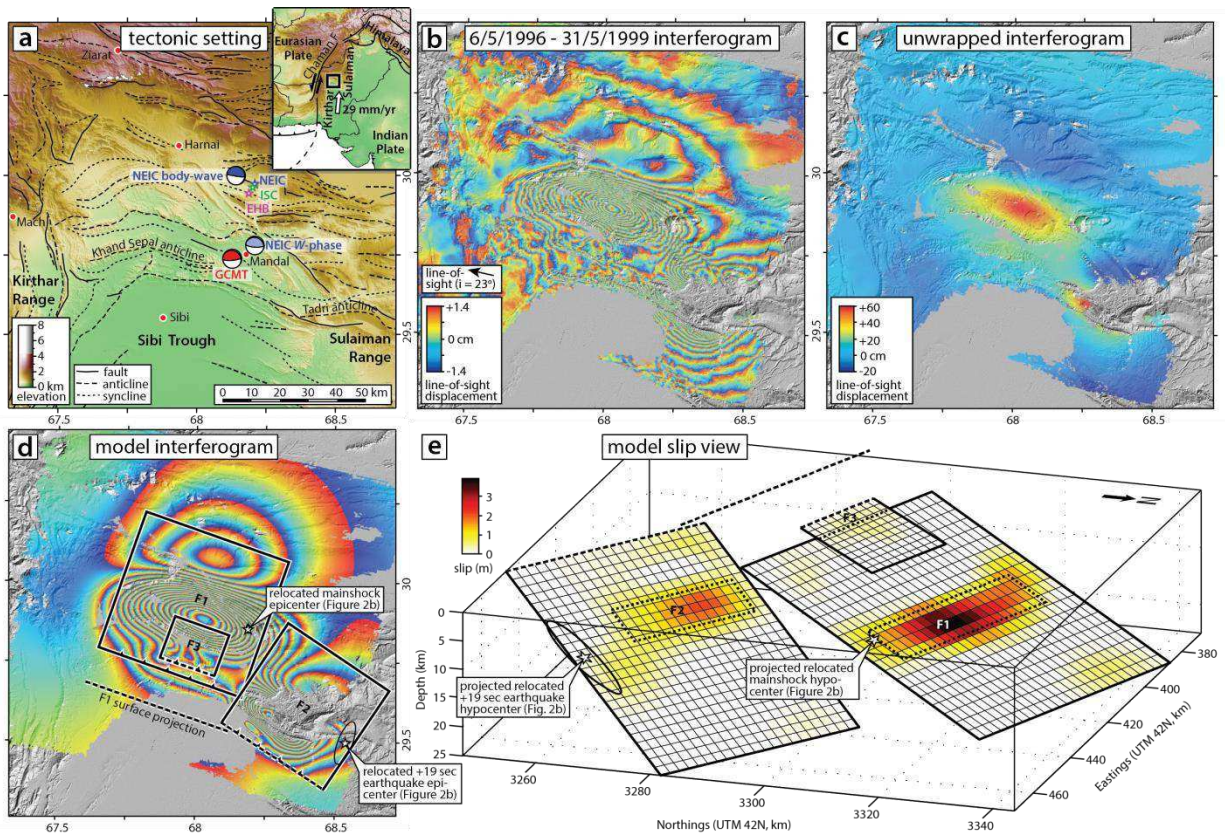


Figure 1 | Tectonic setting and InSAR data and modelling results. (a) Published epicentres and focal mechanisms for the 27 February 1997 earthquake from the USGS National Earthquake Information Center (NEIC, in blue), the International Seismological Centre (ISC, green), the Engdahl, van der Hilst & Bulland catalogue⁴⁹ (EHB, magenta), and the Global Centroid Moment Tensor project (GCMT, red). Inset shows tectonic setting with the local motion of India relative to Eurasia⁵⁰. (b) Wrapped and (c) unwrapped interferogram spanning the mainshock and major aftershocks. (d) Model interferogram and faults, with up-dip surface projections marked by dashed lines. (e) Slip view with extents of initial uniform slip model faults indicated by dotted rectangles.

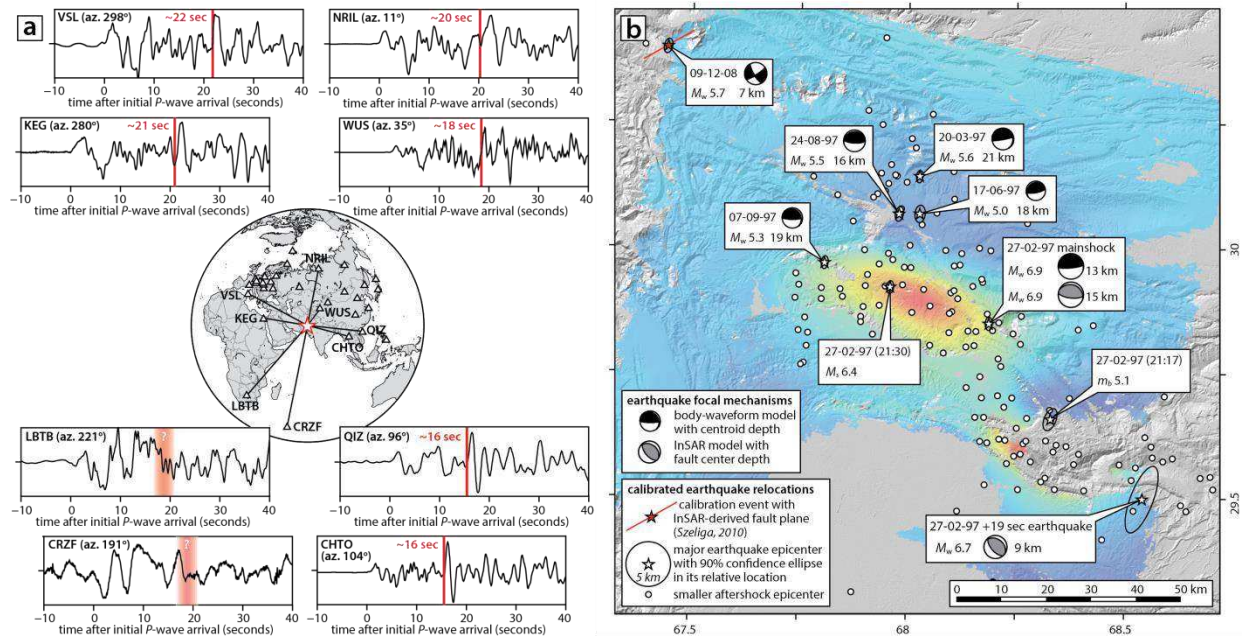


Figure 2 | Seismograms and relocated epicentres. (a) Broadband, vertical component seismograms demonstrating the azimuthal variation in delay between Harnai mainshock and +19 second earthquake P-wave arrivals. LBTB and CRZF are not expected to show impulsive arrivals for the second event. Map shows all stations earthquake relocations in the relocation. (b) Calibrated epicentres for the mainshock, +19 second earthquake, six major aftershocks (stars), and ~150 smaller aftershocks (circles), plotted over the interferogram from Figure 1b. Focal mechanisms from body waveform or InSAR modelling are indicated. To calibrate the cluster we used the 2008 Ziarat earthquake²⁵⁻²⁷, assuming that its epicentre (red star) lies at the centre of an InSAR-derived model fault²⁵ (red line).

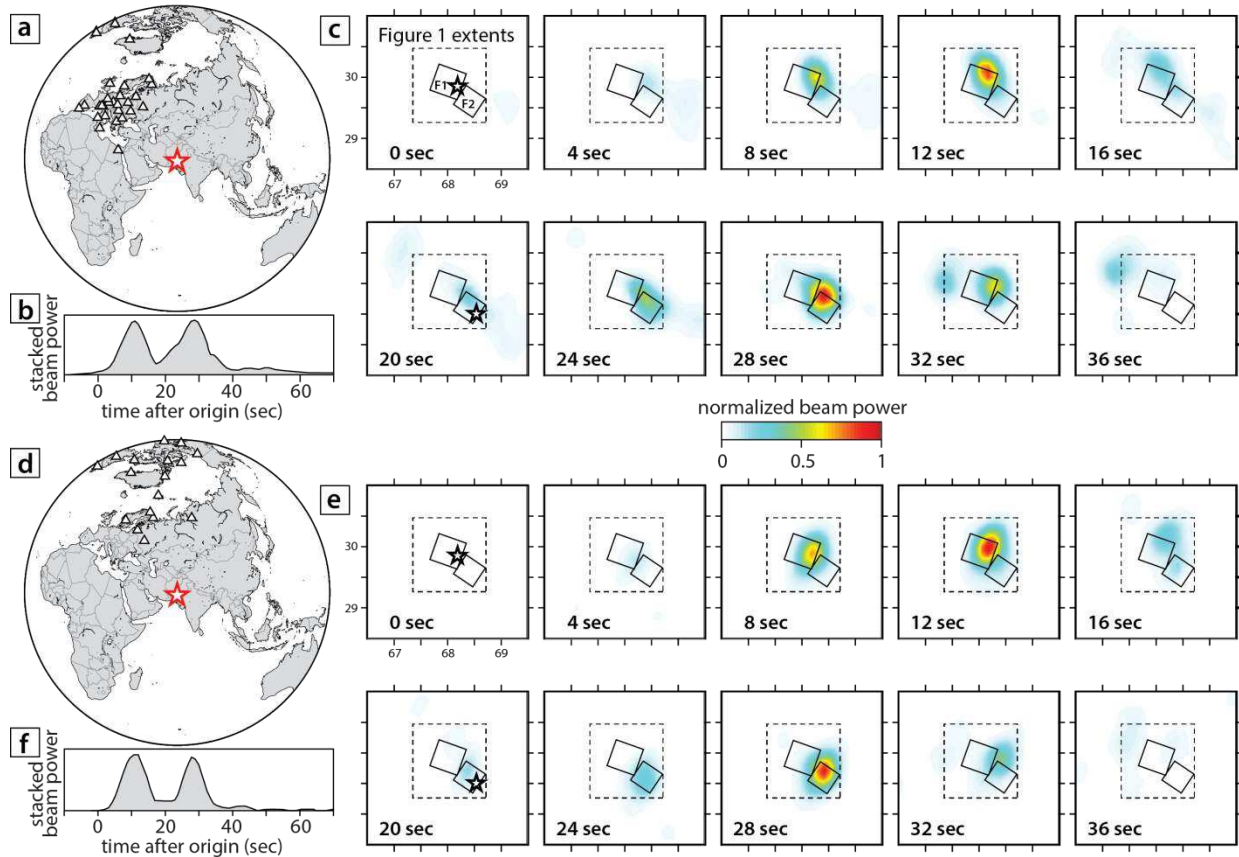


Figure 3 | Seismic back-projections. (a) Back-projection array constructed mostly from European seismic stations. (b) Normalized peak beam power stacked over all grid points. (c) Snapshots of coherent energy plotted at 4 second intervals after the initial rupture. For reference, the stars in the 0 second and 20 second plots indicate the relocated epicentres of the mainshock and +19 second earthquake, respectively (Figure 2b), while the small rectangles outline the F1 and F2 model faults (Figure 1d – e). (d) – (f) Back-projection from an array constructed mostly from North American stations, with details as in (a) – (c).

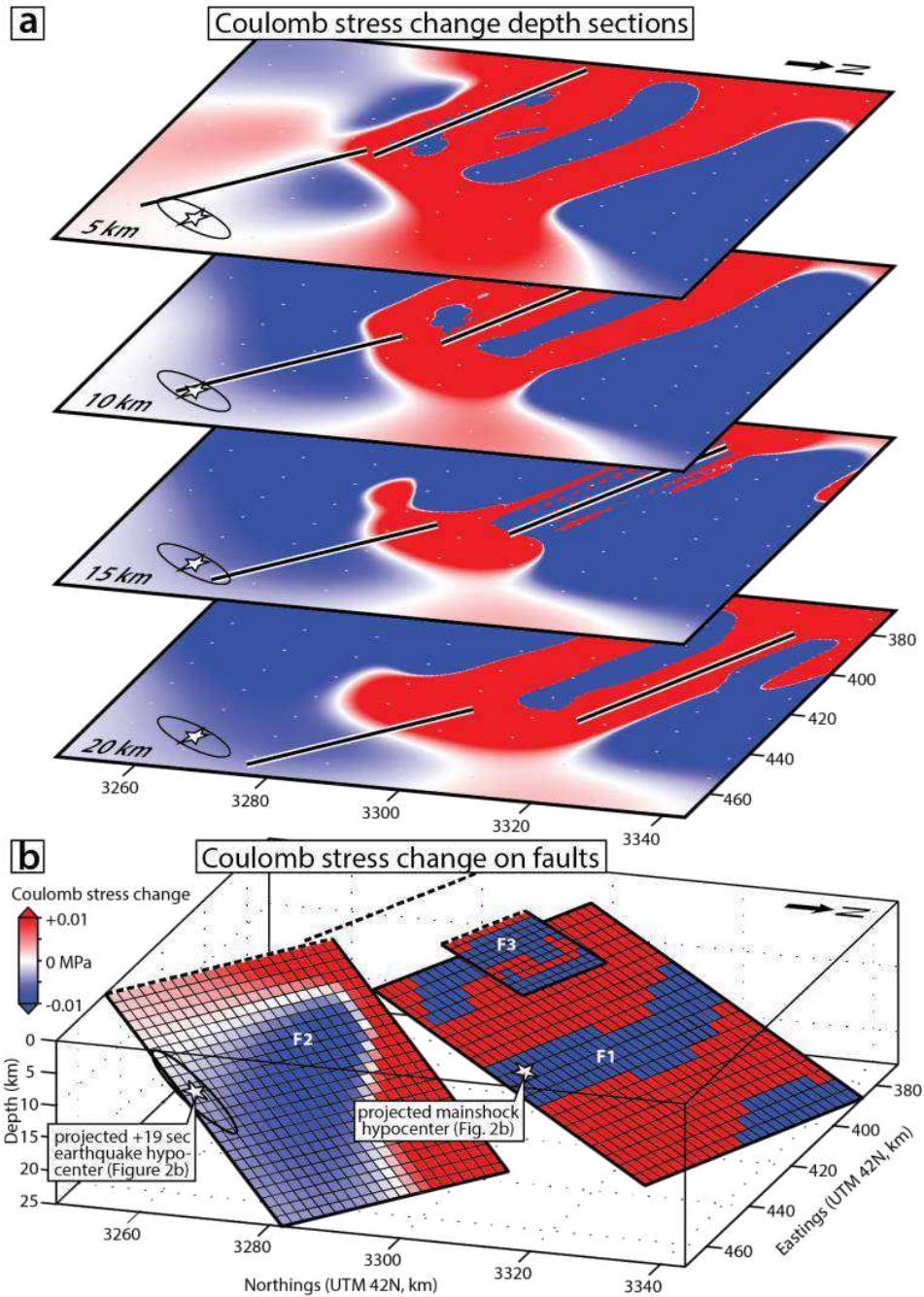


Figure 4 | Coulomb stress changes. (a) Coulomb stress changes caused by slip on NE-dipping source fault F1 at 5 km depth intervals for receiver faults with the same orientation as F2. The +19 second earthquake epicentre is plotted with the 90% confidence ellipse in its relative location (Figure 2b); its hypocentre depth is probably 11 – 17 km. (b) Coulomb stress change resolved onto each receiver fault caused by slip on source fault F1.

Methods

InSAR modelling

We used standard elastic dislocation modelling procedures^{17,18} to characterize the faulting observed in the interferogram. Line-of-sight displacements were first resampled using a quadtree algorithm, reducing the size of the dataset whilst concentrating sampling in areas with high deformation gradients. Representing faults initially as rectangular dislocations buried in an elastic half-space with Lamé parameters $\mu = \lambda = 3.23 \times 10^{10}$ Pa and a Poisson's ratio of 0.25, we used Powell's algorithm with multiple Monte Carlo restarts to obtain the minimum-misfit strike, dip, rake, slip, latitude, longitude, length, and top and bottom depths of each fault, solving simultaneously for a static shift and displacement gradients in the N-S and E-W directions to account for ambiguities in the zero-displacement level and residual orbital phase ramp. Uncertainties in these parameters were then estimated by modelling datasets perturbed by realistic atmospheric noise^{17,18}.

The broad fringe ellipse in the scene centre can be reproduced by either of two, 39 km-long, M_w 6.9 model faults (labelled F1), the first which dips 22° NE and projects upwards towards the northern Sibi Trough, and the second which dips 63° SW and projects to the surface at the northern edge of the fringe ellipse. Both involve buried reverse slip centred at 15 – 16 km depth, though slip magnitude is poorly constrained due to a strong trade-off with fault width. The south-eastern deformation pattern can also be reproduced by either of two conjugate, M_w 6.7 – 6.8 reverse faults (labelled F2), one which dips 31° NE and projects up-dip towards the Sibi Trough, the other which dips 57° SW and projects to the surface north of the Tadri

anticline. Model interferograms and residual (model minus observed) displacements for all four uniform slip F1 and F2 fault combinations are shown in Supplementary Figure 2, with model parameters given in Supplementary Table 2. However, later we will show that only the NE-dipping F1 and F2 model faults are consistent with teleseismic body-waveform analysis and epicentral relocations. Parameter trade-offs and errors for these NE-dipping model faults are shown in Supplementary Figures 3 and 4.

To explore the slip patterns in more detail, we extended each model fault by a few kilometres beyond their uniform slip bounds, and solved for the distribution of slip over these surfaces using a Laplacian smoothing criterion to ensure realistic slip gradients^{17,18}. Fault rakes were fixed to their uniform slip values, reflecting the single available look direction, and a non-negative least squares algorithm was used to prevent retrograde displacements. The trade-off between slip magnitude and down-dip fault width means that there is no unique solution; instead, a suite of models is generated using a range of smoothing parameters. The preferred model was generated using a scalar smoothing factor of 400 to weight the smoothing¹⁸ (Figure 1d – e; residual displacements shown in Supplementary Figure 5c). The F1 slip patch is ~50 km in length, ~15 km in width (its rather elongate dimensions a robust feature of the inversion), centered at ~15 km depth, and has a M_w of 7.0. The F2 slip patch is ~35 km in length, centred at ~9 km depth, with a M_w of 6.8. Its width is less well-resolved due in part to interferometric decorrelation in its hanging wall. Residuals in the areas between the two faults are negligible, implying an absence of slip in the area between the main F1 and F2 slip patches. We also find that additional reverse slip on a third, subsidiary structure is required to fit a minor, E-W phase

discontinuity in the southern part of the central fringe pattern. This M_w 6.1 model fault (labelled F3 in Figure 1d, e) is ~ 20 km long, dips 18° N and extends from close to the surface to a depth of ~ 5 km.

Calibrated earthquake relocations

We used a calibrated earthquake relocation technique^{23,24} to relocate the epicentres of the Harnai mainshock and 150 of its aftershocks. Multiple-event relocations exploit the fact that while unknown velocity structure along teleseismic ray paths leads to large uncertainties in absolute hypocentre positioning, phases from clusters of nearby earthquakes sample roughly the same portion of the Earth, permitting much tighter constraints on *relative* hypocentre locations. If the hypocentre of any one (or more) event in the cluster is known independently, the locations for the entire cluster can be calibrated by applying a shift to satisfy these additional constraints. Earthquakes with moderate source dimensions mapped with InSAR are well-suited for calibration purposes²⁴. In this instance, we exploit a M_w 5.7 strike-slip earthquake which occurred on 9th December 2008 near Ziarat (NW corner of Figure 1) and which exhibits a clear, well-defined InSAR signal consistent with a vertical or sub-vertical fault with a strike of $242^\circ - 245^\circ$ and a length of $8 - 13$ km²⁵⁻²⁷. We take the centre of a uniform slip model fault²⁵ as its epicentre, resulting in a ~ 6.5 km uncertainty in the along-strike direction. This earthquake is spatially separated from the main cluster by several tens of kilometres, and lateral variations in the velocity structure within this region may be an additional source of error. To relocate events in the cluster we used the phase arrival times reported in the ISC bulletin. However, the +19 second aftershock was not reported by the ISC and we instead

manually picked P arrivals from 30 stations at regional and teleseismic distances. We purposely avoided using seismograms at distances $<20^\circ$, since many of these contain complex, refracted head waves which make picking the aftershock arrival difficult. It was also difficult to identify this phase in traces from stations to the SW, probably because the P arrival is near-nodal at teleseismic distances in this direction, and also from Indian Ocean stations which are noisy. Consequently the confidence ellipse for this event is elongated in the SSW-NNE direction. During the relocation we excluded the smallest aftershocks for which there were few reported phase arrivals and an insufficient azimuthal coverage to obtain stable epicentres, and we made an empirical estimate of the average reading error for each station-phase pair and 'cleaned' the ISC phase arrival times of clear outliers. The lack of local phase arrival data prevents us from attempting to constrain the hypocentral depths. Our reported locations (Supplementary Table 3) have been determined assuming 15 km hypocentral depths, close to the base of the seismogenic layer in this region^{13,15}, but using 10 km or 20 km does not significantly change the resulting pattern. Projected onto the NE-dipping F2 model fault plane, the +19 second aftershock hypocentre coincides on a prominent slip patch at 11 – 17 km depth (Supplementary Figure 5a – c). Projected onto the conjugate SW-dipping F2 model fault, the epicentre lies outside the main slip distribution (Supplementary Figure 5d – f), and consequently we are able to discount this candidate fault plane.

Teleseismic body-waveform modelling

Modelling long period teleseismic body waveforms provides independent source parameters for the Harnai mainshock and many of its largest aftershocks. In this approach, earthquakes

appear as a point source in space (the ‘centroid’) and are thus insensitive to short-wavelength variation in fault slip and local velocity structure²⁸. By accounting for the separation between direct P and S arrivals and near-source surface reflections pP , sP and sS , these methods are known to yield more accurate centroid depths than the solutions reported by the GCMT, NEIC or EHB earthquake catalogues, as well as independent estimates of other focal parameters. In some instances teleseismic body waveform modelling can also reveal distinct sub-events and constrain their timing, depths and mechanisms. We used long period (15 – 100 second) seismograms recorded over the distance range $30^\circ - 90^\circ$ (Supplementary Figure 8). Vertical components were used to model P , pP and sP phases and transverse component seismograms were used for the S and sS phases. Without direct measurements of seismic wave velocities in our region of interest, we assumed a half-space with values of 6.0 km/s for the P -wave velocity, 3.5 km/s for the S -wave velocity and $2.8 \times 10^3 \text{ kg/m}^3$ for density, consistent with the elastic half-space structure used in the InSAR modelling. Faster seismic velocities above the earthquake source would result in a shallower centroid depth (and vice versa), whilst the choice of density primarily affects the seismic moment. We used a routine modelling procedure^{19,20} that minimizes the misfit between observed and synthetic seismograms to solve for the best-fit strike, dip, rake, scalar moment, centroid depth and source time function of each event. Uncertainties in key parameters of interest were estimated by holding them fixed, inverting for remaining free parameters, and inspecting the degradation in fit between observed and synthetic waveforms²⁸.

For the initial earthquake, we obtained a good fit to the first ~20 seconds of the observed waveforms, providing important additional constraints on mainshock mechanism and depth (Figure 2b; Supplementary Table 1 and Supplementary Figure 9), but we could not find a stable two-source solution that would also characterize the +19 second aftershock. The gently NE-dipping mainshock nodal plane strike is relatively poorly constrained at $315^{\circ} \begin{smallmatrix} +20^{\circ} \\ -40^{\circ} \end{smallmatrix}$, trading off against rake ($140^{\circ} \begin{smallmatrix} +20^{\circ} \\ -40^{\circ} \end{smallmatrix}$) to keep a relatively stable slip vector ($176^{\circ} \pm 2^{\circ}$). Within error, this strike thus agrees within that of the NE-dipping candidate F1 fault (290°), and our preferred body-wave solution incorporates the more tightly-constrained InSAR-derived strike as a fixed parameter. The strike of the steeper, ~S-dipping body-waveform model nodal plane is $86^{\circ} \begin{smallmatrix} +5^{\circ} \\ -6^{\circ} \end{smallmatrix}$, in clear disagreement with that of the equivalent candidate F1 fault (107°). On this basis we rule out the SW-dipping fault plane. The NE-dipping nodal plane dips at $14^{\circ} \begin{smallmatrix} +8^{\circ} \\ -6^{\circ} \end{smallmatrix}$, just within error of the InSAR-derived F1 dip of 22° . The centroid depth of $13 \text{ km} \begin{smallmatrix} +1 \text{ km} \\ -4 \text{ km} \end{smallmatrix}$ trades off against the moment of $2.5 \begin{smallmatrix} +0.9 \\ -0.3 \end{smallmatrix} \times 10^{19} \text{ Nm}$, both agreeing to within error with the uniform slip F1 values from initial InSAR modelling. The 20 second duration of the source time function is an especially robust feature of the inversion, closely matching that of the first pulse in the back-projection stacked beam power (Figure 3b, 3f). When combined with the ~50 km F1 fault length and the unilateral (SE to NW) rupture propagation direction, this result yields an estimated rupture velocity of ~2.5 km/s. We attempted to characterize the seismograms with a two-source event, fixing the parameters described above for an initial mainshock and then solving for the source parameters (including the azimuth, distance and time delay) of a sub-

event. Though the fit between observed and model seismograms can be improved substantially compared to the single-event model, we find that the sub-event mechanism, depth, and time delay are all highly unstable in this inversion. We are therefore unable to provide seismological constraints on the +19 second aftershock focal mechanism that are independent of the InSAR modelling, as we did for the mainshock.

Source parameters obtained for the largest aftershocks of the Harnai earthquake (Figure 2b; Supplementary Table 4, Supplementary Figures 10 – 14) are similar to those obtained previously using body waveform modelling¹⁵, with discrepancies of at most a few degrees in strike, dip and rake, and up to 2 km in centroid depth. The largest aftershock (4 March 1997, M_w 5.6) was a strike-slip event which occurred SE of the map extents of Figure 2b. The 20 March (M_w 5.6), 17 June (M_w 5.0), 24 August (M_w 5.5) and 7 September 1997 (M_w 5.3) aftershocks have shallow ($12^\circ - 27^\circ$) N- or NNE-dipping nodal planes with slip vectors ($170^\circ - 183^\circ$) that cluster around that of the Harnai mainshock (176°). Unfortunately seismograms of the 27 February 1997 21:17 UTC (m_b 5.1), 21:30 UTC (M_s 6.4) and 22:41 (m_b 5.2) aftershocks were very noisy, preventing us from obtaining robust solutions for these events.

Data and Code availability

ERS-2 SAR data are copyrighted by the European Space Agency and the raw SLC imagery may be obtained from them upon request. InSAR processing was performed using *ROI_PAC* 3.0 software which is freely available from JPL/Caltech (http://www.openchannelfoundation.org/projects/ROI_PAC). Derived interferograms,

corresponding metadata and codes for InSAR modelling are available from the authors upon request. Coulomb stress modelling was performed using *Coulomb 3* software which is freely available from the USGS (<http://earthquake.usgs.gov/research/software/coulomb/>). Seismic arrival time data were obtained from the Bulletin of the International Seismological Centre (<http://www.isc.ac.uk/iscbulletin/>) and modelled using *mloc* software written by Eric Bergman (<http://www.seismo.com/>). Waveform data were accessed through the Incorporated Research Institutions for Seismology (IRIS) Data Management Center (<http://ds.iris.edu/ds/nodes/dmc/>) and modelled using *MT5* and back-projection codes that are available from the authors upon request.

References

1. Wesnousky, S. G. Predicting the endpoints of earthquake ruptures. *Nature* **444**, 358-360 (2006).
2. Wesnousky, S. G. Displacement and geometrical characteristics of earthquake surface ruptures: Issues and implications for seismic-hazard analysis and the process of earthquake rupture. *Bulletin of the Seismological Society of America* **98**, 1609-1632 (2008).
3. Field, E. H. *et al.* Uniform California Earthquake Rupture Forecast, Version 3 (UCERF3)—The Time-Independent Model. *Bulletin of the Seismological Society of America* **104**, 1122-1180 (2014).
4. Page, M. T., Field, E. H., Milner, K. R. & Powers, P. M. The UCERF3 grand inversion: Solving for the long-term rate of ruptures in a fault system. *Bulletin of the Seismological Society of America* **104**, 1181-1204 (2014).

5. Ambraseys, N. & Bilham, R. Earthquakes and associated deformation in northern Baluchistan 1892-2001. *Bulletin of the Seismological Society of America* **93**, 1573-1605 (2003).
6. Nakata, T., Otsuki, K. & Khan, S. H. Active faults, stress field and plate motion along the Indo-Eurasian plate boundary. *Tectonophysics* **181**, 83-95 (1990).
7. Haq, S. S. & Davis, D. M. Oblique convergence and the lobate mountain belts of western Pakistan. *Geology* **25**, 23-26 (1997).
8. Sarwar, G. & DeJong, K. A. Arcs, oroclines, syntaxes: the curvature of mountain belts in Pakistan. In *Geodynamics of Pakistan*, Geological Survey of Pakistan, 351-358 (1979).
9. Banks, C. J. & Warburton, J. 'Passive-roof' duplex geometry in the frontal structures of the Kirthar and Sulaiman mountain belts, Pakistan. *Journal of Structural Geology* **8**, 229-237 (1986).
10. Humayon, M., Lillie, R. J. & Lawrence, R. D. Structural interpretation of the eastern Sulaiman foldbelt and foredeep, Pakistan. *Tectonics* **10**, 299-324 (1991).
11. Davis, D. M. & Lillie, R. J. Changing mechanical response during continental collision: active examples from the foreland thrust belts of Pakistan. *Journal of Structural Geology* **16**, 21-34 (1994).
12. Jadoon, I. A., Lawrence, R. D. & Shahid Hassan, K. Mari-Bugti pop-up zone in the central Sulaiman fold belt, Pakistan. *Journal of Structural Geology* **16**, 147-158 (1994).
13. Bernard, M., Shen-Tu, B., Holt, W. E. & Davis, D. M. Kinematics of active deformation in the Sulaiman Lobe and Range, Pakistan. *Journal of Geophysical Research* **105**, 13253-13279 (2000).
14. Copley, A. The formation of mountain range curvature by gravitational spreading. *Earth and Planetary Science Letters* **351**, 208-214 (2012).

15. Reynolds, K., Copley, A. & Hussain, E. Evolution and dynamics of a fold-thrust belt: the Sulaiman Range of Pakistan. *Geophysical Journal International* **201**, 683-710 (2015).
16. Macedo, J. & Marshak, S. Controls on the geometry of fold-thrust belt salients. *Geological Society of America Bulletin* **111**, 1808-1822 (1999).
17. Wright, T. J., Lu, Z. & Wicks, C. Source model for the M_w 6.7, 23 October 2002, Nenana Mountain Earthquake (Alaska) from InSAR. *Geophysical Research Letters* **30**, 1974 (2003).
18. Funning, G. J., Parsons, B., Wright, T. J., Jackson, J. A. & Fielding, E. J. Surface displacements and source parameters of the 2003 Bam (Iran) earthquake from Envisat advanced synthetic aperture radar imagery. *Journal of Geophysical Research* **110**, B09406 (2005).
19. Talebian, M. & Jackson, J. A reappraisal of earthquake focal mechanisms and active shortening in the Zagros mountains of Iran. *Geophysical Journal International* **156**, 506-526 (2004).
20. Nissen, E., Tatar, M., Jackson, J. A. & Allen, M. B. New views on earthquake faulting in the Zagros fold-and-thrust belt of Iran. *Geophysical Journal International* **186**, 928-944 (2011).
21. Satyabala, S. P., Yang, Z. & Bilham, R. Stick-slip advance of the Kohat Plateau in Pakistan. *Nature Geoscience* **5**, 147-150 (2012).
22. Copley, A. & Reynolds, K. Imaging topographic growth by long-lived postseismic afterslip at Sefidabeh, east Iran. *Tectonics* **33**, 330-345 (2014).
23. Ritzwoller, M. H., Shapiro, N. M., Levshin, A. L., Bergman, E. A. & Engdahl, E. R. Ability of a global three-dimensional model to locate regional events. *Journal of Geophysical Research* **108**, 2353 (2003).

24. Walker, R. T., Bergman, E. A., Szeliga, W. & Fielding, E. J. Insights into the 1968–1997 Dasht-e-Bayaz and Zirkuh earthquake sequences, eastern Iran, from calibrated relocations, InSAR and high-resolution satellite imagery. *Geophysical Journal International* **187**, 1577-1603 (2011).
25. Szeliga, W., M. Historical and Modern Seismotectonics of the Indian Plate with an Emphasis on its Western Boundary with the Eurasian Plate. *PhD thesis*, University of Colorado (2010).
26. Pezzo, G., Boncori, J. P. M., Atzori, S., Antonioli, A. & Salvi, S.. Deformation of the western Indian Plate boundary: insights from differential and multi-aperture InSAR data inversion for the 2008 Baluchistan (Western Pakistan) seismic sequence. *Geophysical Journal International* **198**, 25-39 (2014).
27. Pinel-Puysségur, B., Grandin, R., Bollinger, L. & Baudry, C. Multifaulting in a tectonic syntaxis revealed by InSAR: The case of the Ziarat earthquake sequence (Pakistan). *Journal of Geophysical Research* **119**, 5838-5854 (2014).
28. Molnar, P. & Lyon-Caen, H. Fault plane solutions of earthquakes and active tectonics of the Tibetan Plateau and its margins. *Geophysical Journal International* **99**, 123-154. (1989).
29. Ishii, M., Shearer, P. M., Houston, H. & Vidale, J. E. Extent, duration and speed of the 2004 Sumatra–Andaman earthquake imaged by the Hi-Net array. *Nature* **435**, 933-936 (2005).
30. Trabant, C. *et al.* Data products at the IRIS DMC: stepping-stones for research and other applications. *Seismological Research Letters* **83**, 846-854 (2012).
31. Stein, R. S. The role of stress transfer in earthquake occurrence. *Nature* **402**, 605-609 (1999).

32. Lin, J. & Stein, R. S. Stress triggering in thrust and subduction earthquakes and stress interaction between the southern San Andreas and nearby thrust and strike-slip faults. *Journal of Geophysical Research* **109**, B02303 (2004).
33. Tibi, R., Wiens, D. A., & Inoue, H. Remote triggering of deep earthquakes in the 2002 Tonga sequences. *Nature* **424**, 921-925 (2003).
34. Hill, D. P. *et al.* Seismicity remotely triggered by the magnitude 7.3 Landers, California, earthquake. *Science* **260**, 1617-1623 (1993).
35. Velasco, A. A., Hernandez, S., Parsons, T. & Pankow, K. Global ubiquity of dynamic earthquake triggering. *Nature Geoscience* **1**, 375-379 (2008).
36. Pollitz, F. F., Stein, R. S., Sevilgen, V. & Bürgmann, R. The 11 April 2012 east Indian Ocean earthquake triggered large aftershocks worldwide. *Nature* **490**, 250-253 (2012).
37. Lin, C. H. Remote triggering of the Mw 6.9 Hokkaido Earthquake as a Result of the Mw 6.6 Indonesian Earthquake on September 11, 2008. *Terrestrial, Atmospheric and Oceanic Sciences* **23**, 283-290 (2012).
38. Voisin, C., Campillo, M., Ionescu, I. R., Cotton, F. & Scotti, O. Dynamic versus static stress triggering and friction parameters: Inferences from the November 23, 1980, Irpinia earthquake. *Journal of Geophysical Research: Solid Earth* **105**, 21647-21659 (2000).
39. Felzer, K. R. & Brodsky, E. E. (2006). Decay of aftershock density with distance indicates triggering by dynamic stress. *Nature* **441**, 735-738.
40. Decriem, J. *et al.* The 2008 May 29 earthquake doublet in SW Iceland. *Geophysical Journal International* **181**, 1128-1146 (2010).

41. Richards-Dinger, K., Stein, R. S. & Toda, S. Decay of aftershock density with distance does not indicate triggering by dynamic stress. *Nature* **467**, 583-586 (2010).
42. Gomberg, J., Bodin, P. & Reasenber, P. A. Observing earthquakes triggered in the near field by dynamic deformations. *Bulletin of the Seismological Society of America* **93**, 118-138 (2003).
43. Pollitz, F. F. & Johnston, M. J. Direct test of static stress versus dynamic stress triggering of aftershocks. *Geophysical Research Letters* **33**, L15318 (2006).
44. Parsons, T. & Velasco, A. A.. On near-source earthquake triggering. *Journal of Geophysical Research* **114**, B10307, (2009).
45. Harris, R. A. & Day, S. M. Dynamic 3D simulations of earthquakes on en echelon faults. *Geophysical Research Letters* **26**, 2089-2092 (1999).
46. Rubin, C. M. Systematic underestimation of earthquake magnitudes from large intracontinental reverse faults: Historical ruptures break across segment boundaries. *Geology* **24**, 989-992 (1996).
47. Meng, L. *et al.* Earthquake in a maze: Compressional rupture branching during the 2012 Mw 8.6 Sumatra earthquake. *Science* **337**, 724-726 (2012).
48. Dolan, J. F. *et al.* Prospects for Larger or More Frequent Earthquakes in the Los Angeles Metropolitan Region. *Science* **267**, 199-205 (1995).
49. Engdahl, E. R., van der Hilst, R. & Buland, R. Global teleseismic earthquake relocation with improved travel times and procedures for depth determination. *Bulletin of the Seismological Society of America* **88**, 722-743 (1998).

50. Argus, D. F. *et al.* The angular velocities of the plates and the velocity of Earth's centre from space geodesy. *Geophysical Journal International* **180**, 913-960 (2010).